Anomalous Hall effect emerging from field-induced Weyl nodes in SmAlSi

Yuxiang Gao,[1,2] Shiming Lei,[1,2,*] Eleanor M. Clements,[3,4] Yichen Zhang,[1,2] Xue-Jian Gao,[5] Songxue Chi,[6] Kam Tuen Law,[5] Ming Yi,[1,2] Jeffrey W. Lynn,[3] and Emilia Morosan[1,2,†]

[1]*Department of Physics and Astronomy, Rice University, Houston, Texas 77005, USA*
[2]*Rice Center for Quantum Materials, Rice University, Houston, Texas 77005, USA*
[3]*NIST Center for Neutron Research, National Institute of Standards and Technology, Gaithersburg, Maryland 20899, USA*
[4]*Materials Science and Technology Division, Oak Ridge National Laboratory, Oak Ridge, Tennessee 37831, USA*
[5]*Department of Physics, Hong Kong University of Science and Technology, Clear Water Bay, Hong Kong, China*
[6]*Neutron Scattering Division, Oak Ridge National Laboratory, Oak Ridge, Tennessee 37831, USA*

(Dated: September 12, 2025)

The intrinsic anomalous Hall effect (AHE) has been reported in numerous ferromagnetic (FM) Weyl semimetals. However, AHE in the antiferromagnetic (AFM) or paramagnetic (PM) state of Weyl semimetals has rarely been observed experimentally. Different mechanisms have been proposed to account for the emergence of AHE from different types of magnetic order. In this paper, we propose a new model that explains the observed AHE in both the AFM and PM states of noncentrosymmetric Weyl semimetal SmAlSi. The newly proposed mechanism is based on magnetic field-induced Weyl node evolution, which qualitatively explains the temperature dependence of the anomalous Hall conductivity (AHC), which displays unconventional power-law behavior in both the AFM and PM states of SmAlSi.

Magnetic Weyl semimetals have garnered a lot of interest in recent years because of the interplay between electronic correlations and topology [1–6]. Magnetism drastically increases the number of possible symmetries, from 230 crystalline space groups to 1651 magnetic space groups if we only consider the commensurate order, allowing for the tunability of topology through the magnetic structure. In magnetic Weyl semimetals, Weyl fermions can mediate magnetic order through nesting between different Weyl pockets [6–10]. Furthermore, the Weyl nodes of different chirality in magnetic Weyl semimetals bring about a wide range of magnetotransport and spectroscopic properties [11–16]. Among these, the anomalous Hall effect (AHE) in Weyl semimetals stands out, especially in contrast to the AHE in normal ferromagnets, *e.g.,* iron [17–21]. In the latter, the spin-orbit interaction and the finite magnetization M give rise to a nonzero AHE, where the anomalous Hall conductivity (AHC) is found to be proportional to M [22]. Although nonzero AHE can occur in most FM systems, it has only recently been revealed in a few AFM Weyl semimetals, an observation that required new models since M = 0 [Fig. 1]. The Weyl nodes can behave as effective magnetic monopoles, generating strong Berry curvature, which, in turn, acts like an effective magnetic field in momentum space. In this scenario, finite M (as in FM order) is no longer required to host nonzero AHE [23–25]. More importantly, there are no models and no experimental observations for AHE in the paramagnetic (PM) state of noncentrosymmetric materials.

Here we report the first observation of AHE in the PM state of a noncentrosymmetric Weyl semimetal SmAlSi, together with a novel mechanism that accounts for this new state, based on the magnetic field displacement of the Weyl nodes to inequivalent points in momentum space. This results in regions with nonzero Chern numbers in the first Brillouin zone. Moreover, the same model explains the AHE in the AFM state of SmAlSi, in contrast to the only other noncentrosymmetric AFM semimetal showing AHE, $CoNb_3S_6$ [26] [Fig. 1(d)], where the mechanism relied on breaking time-reversal symmetry (TRS) in a noncollinear magnetic structure [Fig. 1(a)].

SmAlSi is a member of the noncentrosymmetric class of compounds RAl(Si,Ge) (R = La - Sm) [4, 6, 13, 27–36]. The Weyl points and Kramers nodal lines (KNLs) in the PM state of SmAlSi have been investigated through density functional theory (DFT) calculations, angle-resolved photoemission spectroscopy (ARPES) and angle-dependent quantum oscillation (QO) measurements [35]. In addition to the previous report of the topological Hall effect (THE) in the intermediate-field A phase [34], here we report large AHE in the AFM ground state *and* in the PM state of SmAlSi up to 100 K.

Existing proposals for mechanisms responsible for AHE in AFM materials prove inadequate for noncentrosymmetric compounds, as illustrated by SmAlSi. First-principles calculations [37] demonstrate the possibility of nonzero AHE in AFM materials with noncollinear magnetic structures [Fig. 1(a)]. The noncollinear magnetic structure can spontaneously break TRS. In the kagomé AFM metal Mn_3Ir, the breaking of TRS results in nonzero Berry curvature and nonzero AHC. In the isostructural Mn_3Sn and Mn_3Ge, the Mn magnetic sublattice determines if TRS is broken, which, in turn, determines if there is nonzero AHE, as illustrated in Fig. 1(a). The magnetic structure of a bipartite lattice (antiparallel magnetic moment pairs) preserves TRS [top, Fig. 1(a)], while the non-coplanar magnetic structure il-

* current affiliation: Department of Physics, Hong Kong University of Science and Technology, Clear Water Bay, Hong Kong, China
† corresponding author: E. Morosan emorosan@rice.edu

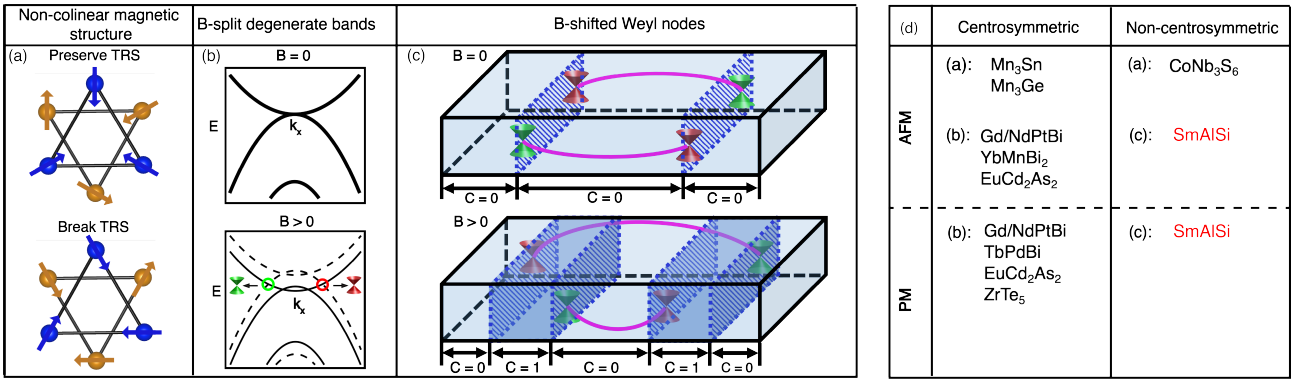

FIG. 1. Proposed AHE mechanisms in antiferromagnets, based on (a) breaking *TRS* in noncollinear magnetic structures, (b) field-split degenerate bands, or (c) field-shifted Weyl nodes. (a) Comparison of two possible AFM magnetic structures that forbid any finite AHE (top panel) or allow finite AHE (bottom panel). (b) Comparison of the band structure of Dirac semimetals without (top panel) and with (bottom panel) applied magnetic field. The magnetic field lifts the band degeneracy and induces Weyl points. (c) Comparison of the band structure of noncentrosymmetric Weyl semimetals without (top panel) and with (bottom panel) applied magnetic field. The Weyl nodes with different chiralities are illustrated in red and green, with Fermi arcs connecting them (magenta curves). The magnetic field changes the position of the Weyl nodes and induces a region with nonzero Chern number (C) in the Brillouin zone. (d) List of well-established centrosymmetric (left) and noncentrosymmetric (right) compounds that exhibit AHE in the AFM state (top) and PM (bottom) state. These compounds are further categorized by the underlying mechanisms in (a-c).

lustrated in bottom, Fig. 1(a) carries a chirality of wind and breaks TRS. If the Weyl points are close to the Fermi energy E_F, the AHE amplitude is enhanced compared to the cases where the Weyl points are away from E_F [38]. Overall, the broken TRS and the Weyl points created by the broken symmetry could explain the observation of the AHE in the ordered state of Mn_3Sn and Mn_3Ge [39, 40]. Similarly, the AHE in the noncentrosymmetric AFM $CoNb_3S_6$ is attributed to the TRS breaking AFM order [26].

In stark contrast to Mn_3Sn and Mn_3Ge, neutron scattering and μSR measurements show that the magnetic order in GdPtBi is collinear AFM below $T_N = 9.2$ K [12, 41]. Despite the lack of inversion center, the electronic structure of GdPtBi in zero field does not feature any Weyl nodes [12, 41]. However, AHE is observed up to 50 K, a temperature significantly higher than T_N. Despite these differences, GdPtBi hosts a nontrivial topology, similar to Mn_3Sn and Mn_3Ge. By breaking TRS through an external magnetic field, the degeneracy of the electronic bands is lifted through the exchange interaction between the Gd ions [11, 12]. As illustrated in Fig. 1(c), the combination of Zeeman effect and magnetic exchange interaction splits the electronic bands, leading to the formation of Weyl nodes in GdPtBi [11, 12]. This mechanism is responsible for the observed AHE in GdPtBi and other centrosymmentric PM compounds [11, 12, 23, 41, 46, 47] including TbPdBi, $EuCd_2As_2$, and $ZrTe_5$ [Fig. 1(d)].

Weyl nodes can occur in noncentrosymmetric materials even in the absence of applied magnetic fields, as is the case in *R*Al(Si,Ge) [27, 28]. In *I*-breaking Weyl semimetals, if TRS is preserved, Weyl nodes with different chiralities appear at opposite momenta, and all regions in the first Brillouin zone have zero Chern number, such that the AHE is expected to be zero [top, Fig. 1(c)]. When FM order or an applied magnetic field breaks TRS [27], the Weyl nodes are effectively shifted by the exchange interaction, resulting in nonzero integration of the Berry curvature. As a result, there are regions with nonzero Chern number in the first Brillouin zone [bottom, Fig. 1(c)], leading to nonzero AHE. Notably, the Zeeman energy is typically significantly smaller than the magnetic exchange energy. Therefore, the AHE resulting from this mechanism is expected to be substantially smaller in NM materials compared to magnetic materials. In the magnetic system SmAlSi, we expect a nonzero AHE even in the PM state, particularly within the temperature range just above T_N. The mechanism proposed here for SmAlSi can be applied to a broad range of noncentrosymmetric Weyl semimetals.

To illustrate the difference between the well-established compounds that exhibit AHE in the AFM state and the PM state, we categorize them by: (1) presence of inversion symmetry, (2) type of magnetic state that exhibits AHE, (3) underlying AHE mechanism [Fig. 1(d)]. The AHE in SmAlSi reported in this work benchmarks this as the first noncentrosymmetric compound that exhibits AHE in the PM state.

Our earlier work has shown that SmAlSi orders antiferromagnetically below $T_N = 11.3$ K and undergoes a second magnetic transition at $T_1 = 4.1$ K [35]. Recent neutron scattering measurements by Yao *et al.* revealed the incommensurate nature of the AFM magnetic order below T_N [34]. Magnetic Bragg peaks were found at $\mathbf{Q}$ = (1/3-δ, 1/3-δ, 4) and (1/3-δ, 1/3-δ, 8), which could be indexed by a propagation vector $\mathbf{k}$ = (1/3-δ, 1/3-δ, 0) with $\delta = 0.007(7)$. We also carried out diffraction mea-

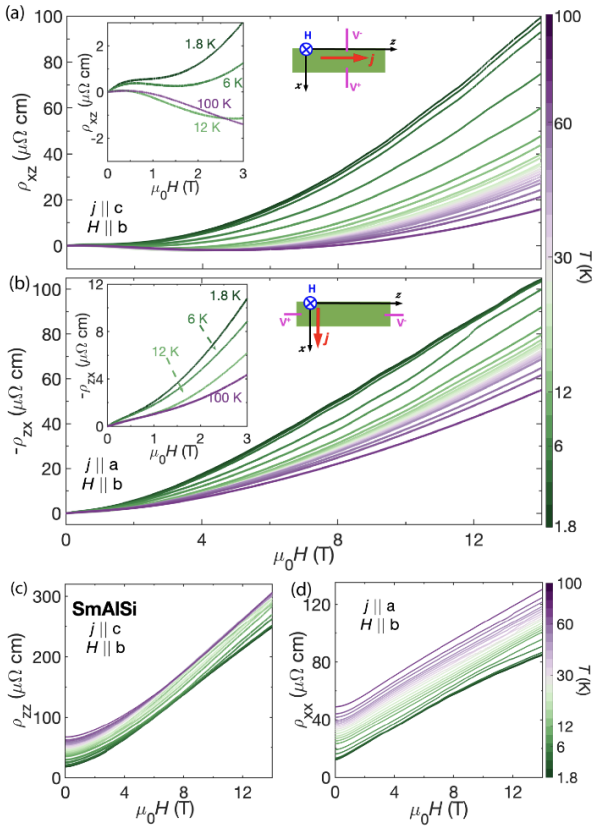

FIG. 2. Transverse resistivity (ρ_{xz} and ρ_{zx}) longitudinal resistivity (ρ_{zz} and ρ_{xx} of SmAlSi). (a, b) Field-dependent Hall resistivity ρ_{xz} and ρ_{zx}, with current $j \parallel c$ and magnetic field $H \parallel b$ (a) and current $j \parallel a$ and magnetic field $H \parallel b$ (b), respectively. The schematics of the corresponding Hall resistivity are shown in the inset. (c,d) Field-dependent resistivity ρ_{zz} and ρ_{xx} as a function of magnetic field.

surements and confirmed the basic magnetic order wave vector is (1/3, 1/3, 0) with an ordering temperature of T_N = 11.2(2) K [Fig. S1(a,b)], where the uncertainty represents one standard deviation [42].

Magnetotransport measurements with current along the c/a axis and magnetic field parallel to the b axis revealed large anomalous Hall contributions to the resistivity and conductivity in both the AFM and PM states. In the following discussion, the x/y/z subscripts of the resistivity or conductivity tensors refer to the a/b/c axes of the crystal [Fig. S1(c)], respectively [42]. The nonlinear field-dependent Hall resistivity components ρ_{xz} and ρ_{zx} [Fig. 2(a,b)] indicate the coexistence of electron and hole carriers, consistent with previous studies [6, 30, 33], although these measurements were performed for a different current-field configuration ($j \parallel a$, $H \parallel c$). Surprisingly, the Hall resistivity components ρ_{xz} and ρ_{zx} show an unusual plateau between 0 and 2 T [inset, Fig. 2(a,b)], which was not observed before, likely due to the different measurement configuration [6, 30, 33]. Considering the additive contributions of Hall conductivity [22], we use conductivity (rather than resistivity) analysis to probe the existence of the AHE. Since the c axis is not equivalent to the a or b axes, the conductivity tensor and the resistivity tensor are connected through

$$\begin{bmatrix} \sigma_{xx} & \sigma_{xz} \\ \sigma_{zx} & \sigma_{zz} \end{bmatrix} = \frac{1}{\rho_{xx}\rho_{zz} - \rho_{xz}\rho_{zx}} \begin{bmatrix} \rho_{xx} & -\rho_{xz} \\ -\rho_{zx} & \rho_{zz} \end{bmatrix} \quad (1)$$

Fig. 2(a,b) shows the measured resistivity data for the relevant current (j) and field (H) orientations, which are used in eq. 1 to estimate the conductivity components σ_{xz} and σ_{zx} [Fig. 3(a,c)]. The unusual plateau between 0 and 2 T in ρ_{xz} develops into an additional peak in σ_{xz} and a broad maximum in σ_{zx}.

To rule out a simple multiband explanation for the observed magnetotransport, we performed two-band model fits to capture the low-field anomaly at 1.8 K. An example of such a fitting is shown in Fig. S5 (dashed lines) for n_1 = 1.08*10^{20}cm^{-3}, μ_1 = 606 cm^{2}V^{-1}s^{-1} and n_2 = 5.36*10^{17}cm^{-3}, μ_2 = 30436 cm^{2}V^{-1}s^{-1} [42]. However, the best fits do not capture the Hall conductivity well for the entire field range. In addition, the conductivity from the fit $\sigma_{xx}^{fit}(H = 0) = n_1 e\mu_1 + n_2 e\mu_2$ = 1.31*10$^4\Omega^{-1}$cm^{-1} is significantly smaller than the experimental value $\sigma_{xx}(H = 0)$ = 8.18*10$^4\Omega^{-1}$cm^{-1}. These observations suggest that a simple multiband model without the inclusion of an anomalous term is not adequate to account for the Hall conductivity.

For magnetic materials, the Hall conductivity sums up two contributions, if the topological spin texture is not considered: the ordinary Hall effect σ^N, and the AHE σ^A [22]:

$$\sigma_{xz} = \sigma_{xz}^N + \sigma_{xz}^A, \quad (2)$$

where the AHE is proportional to the magnetization M $\sigma_{xz}^A = S_H M$. Assuming the linear field dependence of the Hall resistivity, and a small Hall angle ($\rho_{xz} << \rho_{zz}$), the measured Hall resistivity ρ_{xz} can be written as:

$$\rho_{xz} = R_0 H + S_H \rho_{zz}^2 M. \quad (3)$$

While this formula has been successfully applied to analyze the AHE in many FMs, it fails to describe high-mobility multiband systems. In GdPtBi for example, the field-dependent normal Hall effect is nonlinear due to the multiband transport [12, 41]. Instead, the AHE is estimated by subtracting the scaled Hall resistivity measured far above the AFM ordering temperature (T_N = 9.2 K). Such analysis is valid assuming the carrier density and mobility only slightly vary below this temperature. This may not be the case for SmAlSi. To capture the nonlinear field dependence of the Hall effect, we performed a two-band fit to the high field Hall conductivity data σ_{xz} and σ_{zx}. Example fits are shown as dashed lines in Fig. 3(a,c). The difference between the data and model fits $-\sigma_{xz}^A$ [Fig. 3(b,d)] reflects the AHE contribution. A contour plot of this transport response in the H - T phase diagram is shown in Fig. 4(a). Such AHE map bears a striking resemblance to that established for GdPtBi

[12, 41]: both compounds display a peak at low fields, after subtracting the Hall conductivity fit to the high field data. Moreover, the peak persists far above the AFM transition temperature, although the amplitude is reduced with increasing T. In GdPtBi, the AHE persists up to $\sim$ 50 K when T_N = 9.2 K [12, 41]. By comparison, it persists up to temperatures twice as high $T \sim$ 100 K in SmAlSi, even when the ordering temperature is comparable T_N = 11.3 K. At 1.8 K, σ^A_{xz} and σ^A_{zx} reach 1380 and 1030 $\Omega^{-1}cm^{-1}$, about one order of magnitude larger than the values in GdPtBi ($\sim$ 30 - 200 $\Omega^{-1}cm^{-1}$). The resulting tangent of the anomalous Hall angle, $tan\theta^A_{xz} = \sigma^A_{xz}/\sigma_{xx}$ is 0.017 and $tan\theta^A_{zx} = \sigma^A_{zx}/\sigma_{zz}$ is 0.02, which is about 1/8 to 1/10 of that observed in GdPtBi [12, 41], but comparable to that of CeAlSi (0.02) or PrAlGe (0.025) [30, 36], although the latter systems are both ferromagnets.

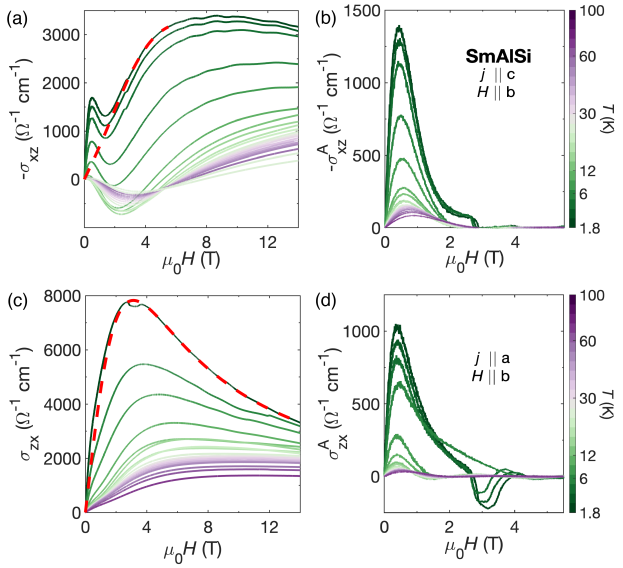

FIG. 3. The AHC of SmAlSi. (a,c) Field-dependent Hall conductivity σ_{xz} and σ_{zx} of SmAlSi. The red dashed lines are the two-band fit ordinary Hall contribution to the Hall conductivity at 1.8 K. (b,d) AHC σ^A_{xz} and σ^A_{zx} as a function of the magnetic field at different temperatures T = 1.8 K to 100 K.

Compared with results from [34] where the Hall anomaly is reported in the finite-field A phase, the Hall anomaly from our Hall conductivity data is found in a much larger temperature range and a distinct magnetic field range. In addition to a different measurement geometry (different current and field direction), the measurements are done on samples with better crystal quality (as demonstrated by heat capacity [35] and quantum oscillations data (Figs. S7-8) [42]. In addition, the differences in the quantum oscillation frequencies and Hall resistivity indicate that the Fermi energy in our samples is lower than in the samples from [34].

The contour map of the AHE contribution in SmAlSi [Fig. 4(a)] shows a striking resemblance to that in GdPtBi [41]. Weyl nodes are expected to play an important role in both systems. Nevertheless, the mechanisms for the formation of the Weyl nodes are quite different. The electronic structure of GdPtBi in zero field does not feature any Weyl nodes. Under a finite field, Weyl nodes form due to the field-induced Zeeman splitting combined with the effect of AFM exchange field.

The AHE in SmAlSi is also significantly different from that in $Mn_3(Ge, Sn)$. In the latter, AHE is observed below the ordering temperature while in the former, it persists well above T_N. At H = 0, the AHE is zero in SmAlSi and nonzero in $Mn_3(Ge, Sn)$. These differences highlight the importance of the magnetic order in $Mn_3(Ge, Sn)$ to induce the AHE, which spontaneously breaks TRS, while in SmAlSi, it is the magnetic field that breaks TRS.

It is necessary to discuss possible Fermi surface reconstruction under a magnetic field in the presence of AHE, as discovered in $YbMnBi_2$ [52]. In $YbMnBi_2$, it has been proposed that the canted Mn moments could change the shape and position of the bands dramatically, such that the energy of the Weyl points relative to the Fermi energy can be tuned, and, in turn, tune the intrinsic anomalous Hall and Nernst effects [52]. It should be noted that the magnetic exchange energy in $YbMnBi_2$ is significantly higher than in SmAlSi: $\mu^{Mn}_{eff} \sim 4\ \mu_B$ with $T_N = 290$ K, and $\mu^{Sm}_{eff} \sim 0.85\ \mu_B$ with $T_N = 11.3$ K, respectively. The exchange energy from the canted Sm^{3+} ions should be too small to significantly impact the Fermi surface topology as in $YbMnBi_2$. In addition, the quantum oscillation frequencies [Fig. S8] do not change across the transitions [42]. Therefore, neither temperature nor field are likely to induce Fermi surface reconstruction in SmAlSi.

We benchmark the AHC in SmAlSi against other established topological semimetals, as indicated by the σ^A_{xz} dependence on σ_{xx} [Fig. 4(b)]. The conductivity of SmAlSi falls in the intrinsic regime, where the interband-coherence-driven intrinsic AHC is independent of the electron scattering mean free time, and should be a constant: $\sigma^A_{xz} \sim$ constant. The amplitude of the AHC is comparable to that of other materials with intrinsic AHE.

The extrinsic skew scattering may contribute to the AHE in SmAlSi as well. In $YbMnBi_2$, the strong anisotropy of the Fermi surface leads to large anisotropy in the conductivity ($\sigma_{bb}/\sigma_{cc} \sim 35$). With H parallel to a, The anomalous Hall and Nernst effects are dramatically enhanced when the current or temperature gradient is parallel to b, as expected for the extrinsic mechanism. In SmAlSi, the conductivity anisotropy is small ($\sigma_{zz}/\sigma_{xx} \sim 1.5$), with similar anomalous Hall conductivity amplitude $\sigma^A_{xz} \sim 1380\ \Omega^{-1}cm^{-1}$ and $\sigma^A_{zx} \sim 1030\ \Omega^{-1}cm^{-1}$.

Apart from the AHE, a non-coplanar spin texture may yield spin chirality, generating Hall anomaly that is usually referred to as THE [53]. We will elaborate on this scenario in the AFM and PM phases of SmAlSi.

Based on the current understanding, it is unclear if any magnetic phases have spin chirality in SmAlSi. Due to the large Sm neutron absorption cross section, neu-

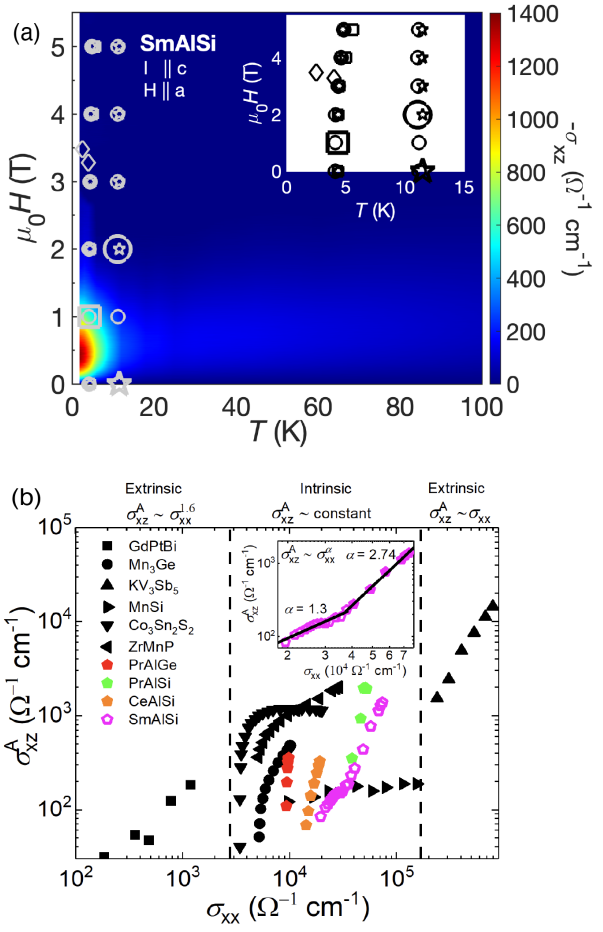

FIG. 4. (a) Contour map of σ^A_{xz} for μ_0H = 0 - 14 T and T = 1.8 - 100 K. The symbols are the phase boundaries determined from Figs. S1-3 , [42]. Inset: a zoomed-in view of the phase diagram at low temperatures. The phase boundaries are determined from the peaks in Cp(T) (stars), d(M(T)/H)/dT (squares), dρ(T)/dT (circles), dM(H)/dH (diamonds). (b) σ^A_{xz} *vs.* σ^A_{xx} for SmAlSi (magenta pentagons), other RAl(Si,Ge) (red, green, and orange pentagons) [30–32], and other topological semimetals (black symbols) [16, 39, 41, 48–50].

tron scattering experiments from [34] and this work only show the basic magnetic order wave vector as (1/3, 1/3, 0) with the magnetic structure undetermined, while the large standard deviation precludes a solid proof of incommensurate order. Moreover, the multi-q feature is missing in the neutron scattering results on SmAlSi, which has been seen as key evidence for non-coplanar spin texture. It is unclear if the magnetic structure establishes spin chirality in SmAlSi as host of skyrmionic correlation.

Skyrmionic correlation could also persist in a small temperature range outside the skyrmion phase, resulting in a vestigial skyrmion lattice phase, as has been shown in MnSi recently [54]. The vestigial phase is limited to a small range close to the skyrmion phase in MnSi, while the Hall anomaly persists in a much larger range well above the ordering temperature. Therefore, it is unlikely that the Hall anomaly in SmAlSi is related to the vestigial skyrmion lattice.

We now turn to the discussion of thermal fluctuations, which, in addition to long-range magnetic order, have been shown to yield finite spin chirality [55, 56]. A competition of thermal fluctuations and Zeeman energy or Dzyaloshinskii–Moriya (DM) interaction has been shown to induce spin chirality in $Gd_3Ru_4Al_{12}$, and in thin film of $SrRuO_3$ and V-doped Bi_2Se_3, respectively [55, 56]. However, as proposed in [56], the fluctuation-driven effect is promoted only when the spin chirality between neighboring plaquettes is not canceled. For lattice motifs with equivalent polygons as in SmAlSi, the fluctuation-driven chirality is expected to cancel out.

It would therefore appear that none of the aforementioned mechanisms are adequate to describe the magnetotransport in SmAlSi. It will be helpful to further explore both the intrinsic and extrinsic contributions to the AHE in SmAlSi, as well as the magnetic structures and magnetic interactions through different theoretical and experimental approaches. The AHE in SmAlSi [Fig. 4(b)] is not a constant as expected for intrinsic deflection [22]. Such behavior is similar to the AHE found in the FMs CeAl(Si,Ge) and PrAl(Si,Ge) [4, 30–32], despite the fact that the AHE is missing in their PM state. Here we provide a qualitative explanation of this dependence, based on a new mechanism.

In our proposed mechanism, the Weyl nodes evolution under an external magnetic field can generate nonzero AHE in noncentrosymmetric systems. Moreover, the AHC has been shown to be proportional to the momentum space separation between Weyl nodes of different chiralities [51]. In SmAlSi, such separation is directly related to the size of the magnetic interaction between the canted Sm^{3+} magnetic moments. A larger moment will induce a larger shift in the electronic bands. The size of the canted moment is reflected in the susceptibility [Fig. S3(a)] or the isothermal magnetization [Fig. S3(c)] [42]. The measurements of both quantities show a negative dependence on temperature, which is consistent with the change in the AHE.

Moreover, the σ^A_{xz} of SmAlSi exhibits two regions that could be differentiated by distinct power-law coefficients, as illustrated by the linear fits in the inset of Fig. 4(b). These two regions coincide with the PM phase (full symbols) and the AFM phase (open symbols). To quantitatively explain this unconventional power-law behavior, extensive theory and experimental work are required to study the AHE dependence under this new mechanism.

We discovered large AHE in both the AFM and PM states of SmAlSi, which is the first observation of AHE in the non-FM state of noncentrosymmetric Weyl semimetals. We propose a new AHE mechanism in noncentrosymmetric Weyl semimetals, based on an external magnetic field breaking T, and shifting the position of the Weyl nodes. Consequently, these Weyl nodes create regions with nonzero Chern number and generate AHE. Our work motivates further studies into the quantitative

understanding of the AHE in SmAlSi and other AFM materials.

This work was primarily supported by the Department of Defense, Air Force Office of Scientific Research under Grant No. FA9550-21-1-0343. S.L. and E.M. acknowledge partial support from the Robert A. Welch Foundation grant C-2114. K.T.L. acknowledges the support of HKRGC through RFS2021-6S03, C6025-19G, AoE/P-701/20, 16307622, 16310520 and 16310219. A portion of this research used resources at the High Flux Isotope Reactor, a DOE Office of Science User Facility operated by the Oak Ridge National Laboratory. The work of EMC (neutron scattering data collection and analysis) was supported by the U.S. Department of Energy (DOE), Office of Science, Basic Energy Sciences (BES), Materials Sciences and Engineering Division. The identification of any commercial product or trade name does not imply endorsement or recommendation by the National Institute of Standards and Technology.

[1] Fujishiro, Y., et al., Giant anomalous Hall effect from spin-chirality scattering in a chiral magnet. *Nat. Commun.* **12**, 317 (2021).
[2] Yang, H., et al., Topological Weyl semimetals in the chiral antiferromagnetic materials Mn_3Ge and Mn_3Sn. *New J. Phys.* **19**, 015008 (2017).
[3] Liu, D. F., et al., Magnetic Weyl semimetal phase in a Kagomé crystal. *Science* **365(6459)**, 1282-1285 (2019).
[4] Puphal, P., et al., Topological Magnetic Phase in the Candidate Weyl Semimetal CeAlGe. *Phys. Rev. Lett.* **124**, 017202 (2020).
[5] Dzsaber, S., et al., Giant spontaneous Hall effect in a nonmagnetic Weyl–Kondo semimetal. *PNAS* **118(8)**, e2013386118 (2021).
[6] Gaudet, J., et al., Weyl-mediated helical magnetism in NdAlSi. *Nat. Mater.* **20**, 1650-1656 (2021).
[7] Lishitz, R., Magnetic point groups and space groups. *arXiv: 0406675* (2022).
[8] Watanabe, H., Po, H. and Vishwanath, A., Structure and topology of band structures in the 1651 magnetic space groups. *Sci. Adv.* **4**, eaat8685 (2018).
[9] Cano, J., Bradlyn, B., and Vergniory, M. G., Multifold nodal points in magnetic materials. *APL Mater.* **7**, 101125 (2019).
[10] Wang, J., et al., NdAlSi: a magnetic Weyl semimetal candidate with rich magnetic phases and atypical transport. *Phys. Rev. B* **105**, 144435 (2022).
[11] Hirschberger, M., et al., The chiral anomaly and thermopower of Weyl fermions in the half-Heusler GdPtBi. *Nat. Mater.* **15**, 1161-1165 (2016).
[12] Shekhar, C., et al., Anomalous Hall effect in Weyl semimetal half-Heusler compounds RPtBi: (R = Gd and Nd). *PNAS* **115(37)**, 9140-9144 (2018).
[13] Sanchez, D., et al., Observation of Weyl fermions in a magnetic noncentrosymmetric crystal. *Nat. Commun.* **11**, 3356 (2020).
[14] Morali, N., et al., Fermi-arc diversity on surface terminations of the magnetic Weyl semimetal $Co_3Sn_2S_2$. *Science* **11**, 3356 (2019).
[15] Li, P., et al., Giant room temperature anomalous Hall effect and tunable topology in a ferromagnetic topological semimetal Co_2MnAl. *Nat. Commun.* **11**, 3476 (2020).
[16] Liu E., et al., Giant anomalous Hall effect in a ferromagnetic kagome-lattice semimetal. *Nat. Phys.* **14**, 1125–1131 (2018).
[17] Feng, J., Pashley, R. and Nicolet, M., Magnetoelectric properties of magnetite thin films. *J. Phys. C: Solid State Phys.* **8**, 1010 (1975).
[18] Taguchi, Y., et al., The spin chirality induced anomalous Hall effect in pyrochlore ferromagnets. *J. Phys.: Condens. Matter* **16**, S599 (2004).
[19] Chun, S. H., et al., Interplay between Carrier and Impurity Concentrations in Annealed $Ga_{1-x}Mn_xAs$: Intrinsic Anomalous Hall Effect. *Phys. Rev. Lett.* **99**, 086602 (2007).
[20] Miyasato, T., et al., Crossover Behavior of the Anomalous Hall Effect and Anomalous Nernst Effect in Itinerant Ferromagnet. *Phys. Rev. Lett.* **99**, 086602 (2007).
[21] Shiomi, Y., Onose, Y. , and Tokura, Y., Extrinsic anomalous Hall effect in charge and heat transport in pure iron, $Fe_{0.97}Si_{0.03}$, and $Fe_{0.97}Co_{0.03}$. *Phys. Rev. B* **79**, 100404 (2009).
[22] Nagaosa, N., et al., Anomalous Hall effect. *Rev. Mod. Phys.* **82**, 1539 (2010).
[23] Tian, L., et al., Anomalous Hall effect in $ZrTe_5$. *Nat. Phys.* **14**, 451-455 (2018).
[24] Armitage, N. P., Mele, E.J. and Vishwanath, A., Weyl and Dirac semimetals in three-dimensional solids. *Rev. Mod. Phys.* **90**, 015001 (2018).
[25] Hu, J., et al., Transport of Topological Semimetals. *Annu. Rev. Mater. Res.* **49**, 207-252 (2019).
[26] Ghimire, N. J., et al, Large anomalous Hall effect in the chiral-lattice antiferromagnetic $CoNb_3S_6$. *Nat. Commun.* **9**, 3280 (2018).
[27] Chang G., et al., Magnetic and noncentrosymmetric Weyl fermion semimetals in the RAlGe family of compounds (R = rare earth). *Phys. Rev. B* **97**, 041104(R) (2018).
[28] Xu SY., et al., Discovery of Lorentz-violating type II Weyl fermions in LaAlGe. *Sci. Adv.* **3**, e1603266 (2019).
[29] Suzuki T., et al., Singular angular magnetoresistance in a magnetic nodal semimetal. *Science* **365**, 377-381 (2019).
[30] Destraz, D. Q., et al., Magnetism and anomalous transport in the Weyl semimetal PrAlGe: possible route to axial gauge fields. *npj Quantum Materials* **5**, 5 (2020).
[31] Lyu, M., et al., Nonsaturating magnetoresistance, anomalous Hall effect, and magnetic quantum oscillations in the ferromagnetic semimetal PrAlSi. *Phys. Rev. B* **102**, 085143 (2020).
[32] Yang, H., et al., Noncollinear ferromagnetic Weyl semimetal with anisotropic anomalous Hall effect. *Phys. Rev. B* **103**, 115143 (2021).
[33] Cao, W., et al., Quantum oscillations in noncentrosymmetric Weyl semimetal SmAlSi. *Chin. Phys. Lett.* **39**, 047501 (2022).
[34] Yao, X., et al., Topological spiral magnetism in the Weyl semimetal SmAlSi. *Phys. Rev. X* **13**, 011035 (2023).
[35] Zhang, Y., et al., Kramers Nodal Lines and Weyl

Fermions in SmAlSi. *Commun. Phys.* **6**, 134 (2023).
[36] Cheng, E., et al., Anomalous transverse transport and phase transitions in Weyl semimetals RAlSi (R = La, Ce). *arxiv:2301.03800* (2023).
[37] Chen, H., Niu, Q. and MacDonald, A. H., Anomalous Hall Effect Arising from Noncollinear Antiferromagnetism. *Phys. Rev. Lett.* **112**, 017205 (2014).
[38] Kübler, J. and Felser, C., Non-collinear antiferromagnets and the anomalous Hall effect. *EPL* **108**, 67001 (2014).
[39] Nayak, A. K., et al., Large anomalous Hall effect driven by a nonvanishing Berry curvature in the noncolinear antiferromagnet Mn_3Ge. *Sci. Adv.* **2**, e1501870 (2016).
[40] Nakatsuji, S.,Kiyohara, N. and Higo, T., Large anomalous Hall effect in a noncollinear antiferromagnet at room temperature. *Nature* **527**, 212-215 (2015).
[41] Suzuki T., et al., Large anomalous Hall effect in a half-Heusler antiferromagnet. *Nat. Phys.* **12**, 1119–1123 (2016).
[42] See Supplemental Material at [URL will be inserted by publisher], which includes Refs. [43-45] for additional experimental data and a detailed discussion on quantum oscillations. .
[43] Wang, J., et al., Quantum oscillations in the magnetic Weyl semimetal NdAlSi arising from strong Weyl fermion–4f electron exchange interaction. *Phys. Rev. B* **108**, 024423 (2023).
[44] Guo, C., et al., Temperature dependence of quantum oscillations from non-parabolic dispersions . *Nat. Commun.* **12**, 6213 (2021).
[45] Lou, R., et al., Signature of weakly coupled f electrons and conduction electrons in magnetic Weyl semimetal candidates PrAlSi and SmAlSi. *Phys. Rev. B* **107**, 035158 (2023).
[46] Zhu, Y., et al., Large anomalous Hall effect and negative magnetoresistance in half-topological semimetals. *Commun. Phys.* **6**, 346 (2023).
[47] Roychowdhury, Si., et al., Anomalous Hall Conductivity and Nernst Effect of the Ideal Weyl Semimetallic Ferromagnet $EuCd_2As_2$. *Adv. Sci.* **10**, 2207121 (2023).
[48] Lee, M., et al., Hidden constant in the anomalous Hall effect of high-purity magnet MnSi. *Phys. Rev. B* **75**, 172403 (2007).
[49] Singh, S., et al., Anisotropic Nodal-Line-Derived Large Anomalous Hall Conductivity in ZrMnP and HfMnP. *Adv. Mater.* **33**, 2104126 (2021).
[50] Yang, S. Q., et al., Giant, unconventional anomalous Hall effect in the metallic frustrated magnet candidate, KV_3Sb_5. *Sci. Adv.* **6**, eabb6003 (2020).
[51] Burkov, A. A., Anomalous Hall Effect in Weyl Metals. *Phys. Rev. Lett.* **113**, 187202 (2014).
[52] Pan, Y., et al., Giant anomalous Nernst signal in the antiferromagnet $YbMnBi_2$. *Nat. Mater.* **21**, 203-209 (2021).
[53] Tokura, Y. and Kanazawa, N., Magnetic skyrmions materials . *Chem. Rev.* **121**, 2857-2897 (2021).
[54] Kindervater, J., et al., Weak Crystallization of Fluctuating Skyrmion Textures in MnSi. *Phys. Rev. X* **9**, 041059 (2019).
[55] Wang, W., et al., Spin chirality fluctuation in two-dimensional ferromagnets with perpendicular magnetic anisotropy. *Nat. Mater.* **18**, 1054-1059 (2019).
[56] Kolincio, K., et al., Kagome Lattice Promotes Chiral Spin Fluctuations. *Phys. Rev. Lett.* **130**, 136071 (2023).